Additive Manufacturing: Metallurgy, Cut Analysis & Porosity

12 Advanced Optical Metrology

Additive Manufacturing:
Metallurgy, Cut Analysis & Porosity

EVIDENT OLYMPUS

WILEY

The latest eBook from Advanced Optical Metrology. Download for free.
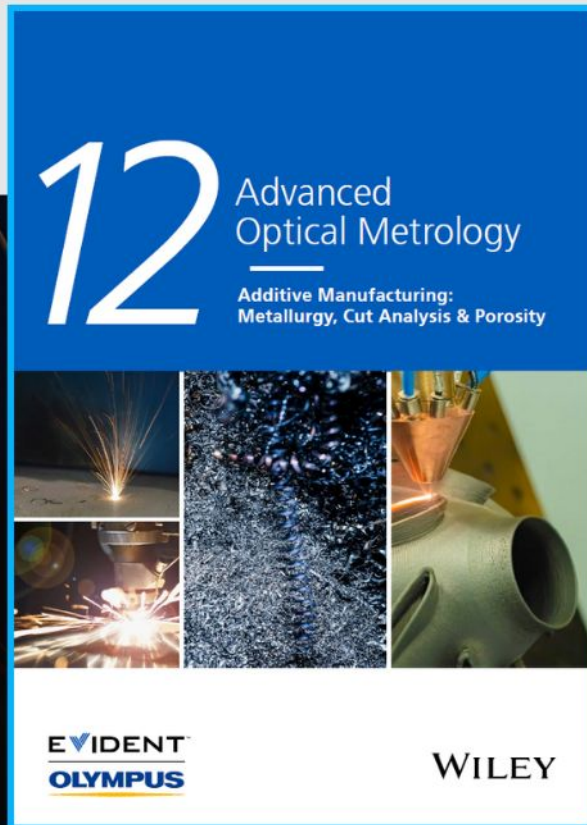
In industry, sector after sector is moving away from conventional production methods to additive manufacturing, a technology that has been recommended for substantial research investment.

Download the latest eBook to read about the applications, trends, opportunities, and challenges around this process, and how it has been adapted to different industrial sectors.

EVIDENT OLYMPUS

WILEY

Biomimetic Lipid-Bilayer Anode Protection for Long Lifetime Aqueous Zinc-Metal Batteries

Yan Zhao, Mengzheng Ouyang, Yuetao Wang, Runzhi Qin, Hao Zhang, Wending Pan, Dennis Y. C. Leung, Billy Wu, Xinhua Liu, Nigel P. Brandon, Jin Xuan,* Feng Pan,* and Huizhi Wang*

The practical application of rechargeable aqueous zinc batteries is impeded by dendrite growth, especially at high areal capacities and high current densities. Here, this challenge is addressed by proposing zinc perfluoro(2-ethoxyethane)sulfonic ($Zn(PES)_2$) as a zinc battery electrolyte. This new amphipathic zinc salt, with a hydrophobic perfluorinated tail, can form an anode protecting layer, in situ, with a biomimetic lipid-bilayer structure. The layer limits the anode contact with free H_2O and offers fast Zn^{2+} transport pathways, thereby effectively suppressing dendrite growth while maintaining high rate capability. A stable, Zn^{2+}-conductive fluorinated solid electrolyte interphase (SEI) is also formed, further enhancing zinc reversibility. The electrolyte enables unprecedented cycling stability with dendrite-free zinc plating/stripping over 1600 h at 1 mA cm^{-2} at 2 mAh cm^{-2}, and over 380 h under an even harsher condition of 2.5 mA cm^{-2} and 5 mAh cm^{-2}. Full cell tests with a high-loading VS_2 cathode demonstrate good capacity retention of 78% after 1000 cycles at 1.5 mA cm^{-2}. The idea of in situ formation of a biomimetic lipid-bilayer anode protecting layer and fluorinated SEI opens a new route for engineering the electrode–electrolyte interface toward next-generation aqueous zinc batteries with long lifetime and high areal capacities.

1. Introduction

The growing share of renewables in the energy mix increases the demand for using large-scale battery storage to balance the grid and store excess energy. Lithium-ion batteries are currently the dominant battery technology, which account for ≈90% of the annual capacity additions for stationary battery storage.[1] However, the long-term concerns about sustainability and safety of lithium-ion batteries have spurred research into alternative battery chemistries which can be safer and use more abundant elements.[2–4] Zinc is an attractive anode material because of its relatively high abundance and low cost. Its bivalence along with the high density give a high theoretical volumetric capacity of 5854 mAh cm^{-3}, compared with 2061 mAh cm^{-3} for lithium and 1129 mAh cm^{-3} for sodium.[5–7] Being water compatible, zinc (Zn) anodes can be coupled with aqueous electrolytes to offer

Y. Zhao, H. Wang
Department of Mechanical Engineering
Imperial College London
London SW7 2AZ, UK
E-mail: huizhi.wang@imperial.ac.uk
M. Ouyang, N. P. Brandon
Department of Earth Science and Engineering
Imperial College London
London SW7 2AZ, UK
Y. Wang, R. Qin, F. Pan
School of Advanced Materials
Peking University Shenzhen Graduate School
Shenzhen 518055, China
E-mail: panfeng@pkusz.edu.cn

H. Zhang
Department of Materials
Imperial College London
London SW7 2AZ, UK
W. Pan, D. Y. C. Leung
Department of Mechanical Engineering
The University of Hong Kong
Hong Kong 999077, China
B. Wu, X. Liu
Dyson School of Design Engineering
Imperial College London
London SW7 2AZ, UK
X. Liu
School of Transportation Science and Engineering
Beihang University
Beijing 100191, China
J. Xuan
Department of Chemical Engineering
Loughborough University
Loughborough LE11 3TU, UK
E-mail: j.xuan@lboro.ac.uk

**ADVANCED
SCIENCE NEWS**

www.advancedsciencenews.com

**ADVANCED
FUNCTIONAL
MATERIALS**

www.afm-journal.de

fast-kinetics, low-toxicity and high safety battery solutions compared to those non-aqueous batteries. However, their practical application is impeded by dendrite growth and poor reversibility of Zn anodes, especially at high areal capacities and high current densities. A fast charge/discharge process can cause the accumulation of a large amount of free moving anions around Zn protrusions and thus the formation of an inhomogeneous electric field, accelerating Zn dendrite growth.[8,9] Operating a Zn battery at high areal capacities can lead to continued dendrite growth, increasing the chance of piercing the separator.

Recent advances in lithium-ion battery electrolytes have shown that the presence of fluorine species in solid–electrolyte interphases (SEI), in the form of simple inorganic fluorides lithium fluoride and organofluoro moieties, can remarkably enhance the reversibility and stability of lithium metal anodes by forming dense and homogenous passivation films.[10–13] A similar strategy has therefore been used for developing Zn battery electrolytes to in situ form fluorinated interphases on Zn anodes, which has demonstrated that this Zn^{2+}-conducting SEI can suppress H_2 evolution while ZnF_2 in the SEI can improve Zn deposition/stripping reversibility. Qiu et al.[14] reported the use of an acetamide-Zinc bis(trifluoromethylsulfonyl)imide $(Zn(TFSI)_2)$ eutectic electrolyte to in-situ form a fluoride-rich organic/inorganic hybrid SEI on the Zn anode, which significantly enhanced Zn deposition/stripping reversibility. Cao et al.[15] triggered in situ formation of a fluorinated and hydrophobic Zn^{2+}-conducting interphase in zinc trifluoromethanesulfonate $Zn(OTF)_2$ electrolytes with trimethylethyl ammonium trifluoromethanesulfonate $(Me_3EtNOTF)$ as an additive, and realized stable charge and discharge in a Zn‖Zn symmetric cell for 6000 h at 0.5 mA cm⁻² and 0.25 mAh cm⁻². Ma et al.[16] used functionalized phosphonium cations to achieve dendrite-free Zn plating/stripping for over 280 h at 2.5 mA cm⁻² by reshaping interfacial structures and interphasial chemistries. Despite the remarkable improvement in Zn stability and reversibility, most of the existing zinc electrolyte studies[14–18] relied on high-concentration electrolytes with areal capacities less than 1 mAh cm⁻², which are far from the commercial requirement of 3 mAh cm⁻².[19]

Inspired by the self-assembly of phospholipid molecules of cell membranes at a gold electrode surface,[20] we address the trade-off between Zn reversibility and areal capacity by proposing a novel amphipathic electrolyte, zinc perfluoro(2-ethoxyethane)sulfonate $(Zn(PES)_2)$, which can form a lipid-bilayer-like protecting layer on the Zn anode surface (**Figure 1**a). In the new electrolyte, the PES anion is an amphipathic compound featuring a hydrophilic sulfonate head and a large hydrophobic perfluorinated carbon chain tail (Figure 1a4). On the one hand, the existence of strongly electron-withdrawing perfluorinated carbon chains results in extensive negative-charge delocalization across the $-SO_3^-$ group of the anion, which weakens its capability of coordination to Zn^{2+} cations and thus ensures good ion dissociation and high ionic conductivity of the electrolyte. On the other hand, the amphipathic nature of the salt enables in situ formation of an anode protecting layer with a biomimetic lipid-bilayer structure composed of a hydrophobic layer of perfluorinated tails and a hydrophilic layer of Zn^{2+} and H_2O (Figure 1a1–3). The hydrophobic layer limits the anode contact with H_2O, and the hydrophilic layer offers fast Zn^{2+}

transport pathways, thereby effectively suppressing dendrite growth while improving rate capability. In contrast to conventional electrolytes where inhomogeneous space electric fields are formed because of free anion accumulation,[9] the PES⁻ anions are uniformly distributed in the gel network structure of the protecting layer without causing an inhomogeneous space electric field, while Zn^{2+} cations and water molecules are confined in the hydrophilic channels, which avoids tip growth of dendrites and hydrogen evolution (Figure 1b). A stable, Zn^{2+}-conductive fluorinated SEI is also formed, further enhancing Zn reversibility.

The electrolyte suppresses dendrite growth for over 7000 h at 0.25 mA cm⁻² at 0.5 mAh cm⁻². It is able to deliver dendrite-free Zn plating/stripping for over 1600 h at a high current density of 1 mA cm⁻² and high areal capacity of 2 mAh cm⁻², and for over 380 h under an even harsher condition of 2.5 mA cm⁻² and 5 mAh cm⁻², which are the highest values in the aqueous zinc electrolyte studies reported to date with such high areal capacities and high current densities. The advantages of the new electrolyte were further demonstrated in full Zn-ion battery cells with a VS_2@stainless steel (SS) cathode, which showed reversible specific capacity of 140.5 mAh g⁻¹ and a good capacity retention of 78% after 1000 cycles at 1.5 mA cm⁻² even at a high loading of cathode materials (7.5 mg cm⁻²). The idea of in situ formation of biomimetic lipid-bilayer anode protection and fluorinated SEI from $Zn(PES)_2$ electrolytes opens a new route for engineering the electrode–electrolyte interface toward next-generation aqueous Zn batteries with long life and high areal capacities.

2. Results and Discussion

2.1. The Physico-Chemical Properties of $Zn(PES)_2$ Electrolytes

As an ionic surfactant, $Zn(PES)_2$ can self-assemble into bilayers when exceeding a certain concentration.[21] As shown in the bottom panel of **Figure 2**a, the $Zn(PES)_2$ solution at 0.2 m is clear and transparent with no obvious Tyndall effect, suggesting that the $Zn(PES)_2$ salt in the dilute solution mainly exists in the form of ion pairs. With the increase of salt concentration, the salt begins to aggregate to form micelle aggregates, where the hydrophobic tails form the core of the aggregate and the hydrophilic heads are in contact with the surrounding liquid,[21] resulting in a strong Tyndall effect at concentrations >1 m. With a further increase in salt concentration, the interactions between different micelle aggregates begin to be strengthened due to improved coulomb interactions between Zn^{2+} cation mediums and hydrophilic anionic heads derived from the shorter interactive distance between micelle aggregates. As the concentration reaches above its critical value of 1.35 m, more interactive points between micelle aggregates occur and partial micelle aggregates restructure to form bilayer arrangements, the whole solution turns into a solid gel phase with a continuous network structure. The Tyndall effect with an apparent anisotropy at 1.35 m indicates the existence of lipid-bilayer-like structures.

The unique solution structures endow $Zn(PES)_2$ electrolytes with high ionic conductivities despite of increased viscosities
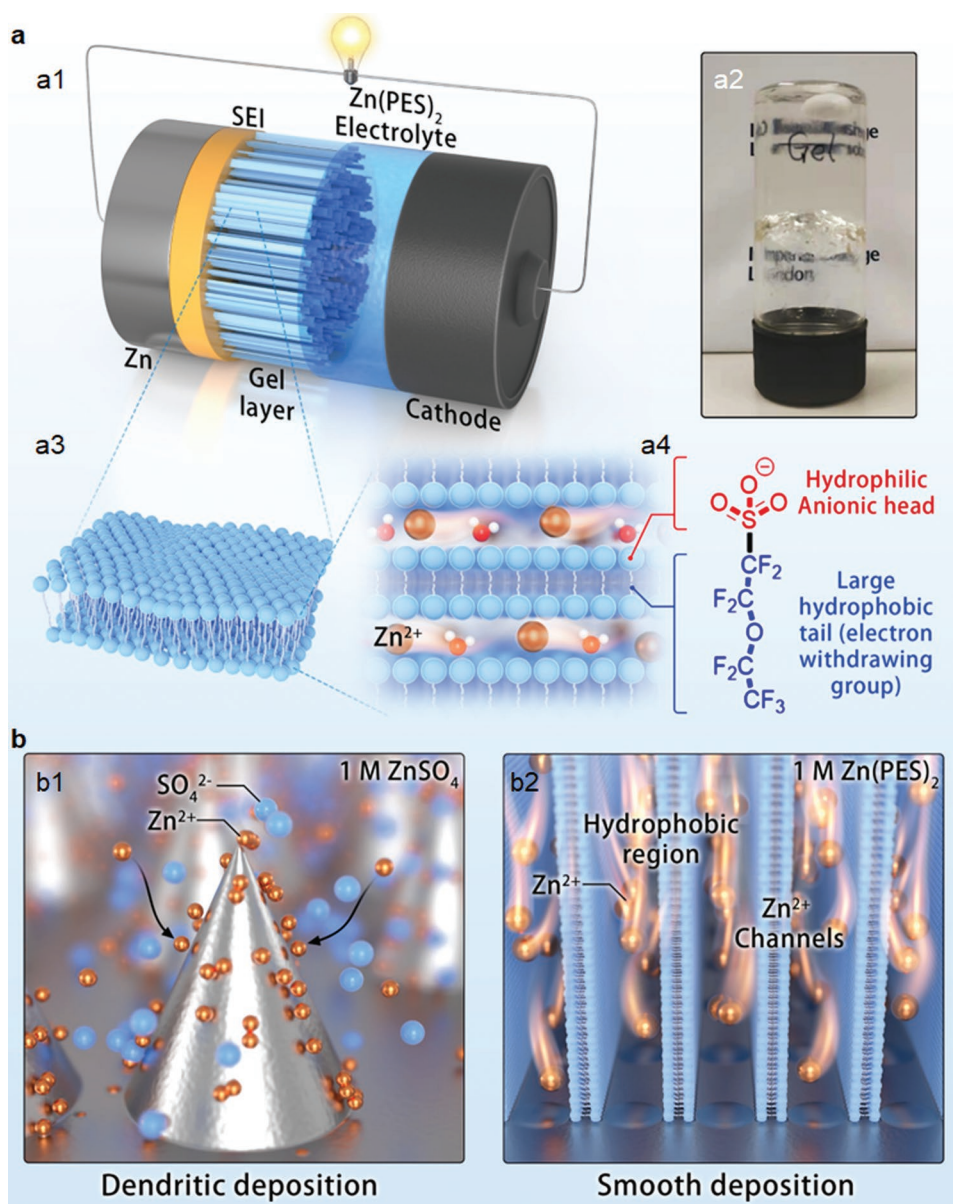
**ADVANCED
SCIENCE NEWS**
www.advancedsciencenews.com

**ADVANCED
FUNCTIONAL
MATERIALS**
www.afm-journal.de

Figure 1. a) The schematic of the protecting layer formation from Zn(PES)$_2$ electrolyte: a1) In situ formed biomimetic lipid-bilayer protecting layers and SEI in Zn ion batteries, a2) a photo of the gel electrolyte containing bilayer structures, a3) structure details of biomimetic lipid-bilayer protecting layers, and a4) the molecule structure of PES$^-$ anion. b) The schematic of the Zn plating process in b1) ZnSO$_4$ electrolytes and b2) Zn(PES)$_2$ electrolytes.

(Figure 2b). It is found that the viscosity increases exponentially with increasing salt concentration. The viscosity value of 1 M Zn(PES)$_2$ solution is 15.3 mPa s, which is ten times that of 1 M ZnSO$_4$ solution (1.55 mPa s) (Figure S1, Supporting Information). However, the ionic conductivity of the Zn(PES)$_2$ solution increases with increasing salt concentration and reaches the maximum value of 51.9 mS cm^{-1} at 1 M, suggesting that the highest mobile ion number is reached at 1 M despite of the significantly increased viscosity. As the salt concentration further increases to 1.2 M, the ionic conductivity slightly decreases, indicating that viscosity becomes a dominating factor on the ionic conductivity. At 1.35 M where gelation occurs, despite a viscosity higher than 1500 mPa s (Figure S2, Supporting Information), a high ionic conductivity of 49.2 mS cm^{-1} (vs 49.2 mS cm^{-1}

for 1.2 M dilute Zn(PES)$_2$ solution, or 47.9 mS cm^{-1} for 1 M dilute ZnSO$_4$ solution) is still maintained, suggesting the existence of fast ion transport pathways within the solid gel phase.

Figure 2c shows the Raman spectra of the Zn(PES)$_2$ electrolyte as the concentration increases. The pure Zn(PES)$_2$ powders give a strong peak around 1069 cm^{-1}, which can be ascribed to the symmetric stretch of -SO$_3^-$ group due to its strong interaction with Zn^{2+} cations.[22,23] In its dilute solution (0.2 M), no signal at 1069 cm^{-1} is observed and a new signal peak at 1059 cm^{-1} occurs, suggesting the salts dissociate completely and the anions exist in the solution in the form of the free anions. The signal shifts slightly with the increase of salt concentration to 1 M, which can be ascribed to the stronger interaction between cations and anions, indicating the decrease of free anions and
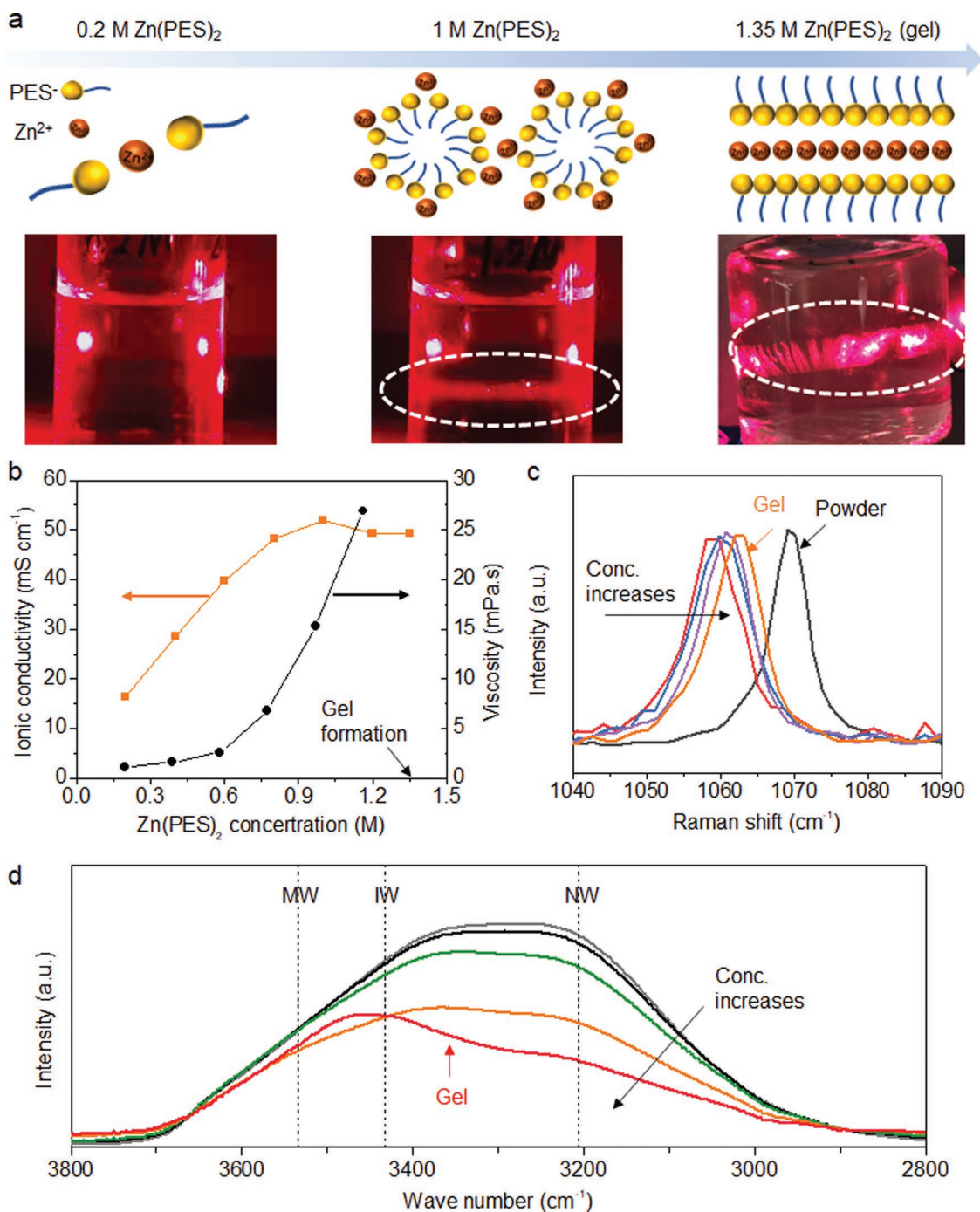
**ADVANCED
SCIENCE NEWS**

www.advancedsciencenews.com

**ADVANCED
FUNCTIONAL
MATERIALS**

www.afm-journal.de

Figure 2. a) The schematic diagram of the structure evolution of Zn(PES)$_2$ with an increasing concentration. b) Variations of viscosity and ionic conductivity with the electrolyte concentration. c) Raman spectra between 1040 and 1090 cm^{-1} (−SO$_3^-$ the symmetric stretching vibration of PES$^-$ anions) for different electrolyte concentrations (0.2, 0.6, 1.0, and 1.35 M (gel)) and Zn(PES)$_2$ powders. d) FTIR spectra of Zn(PES)$_2$ electrolytes at different concentrations (0 (water), 0.2, 0.6, 1.0, and 1.35 M (gel)).

increase of loose ion pairs. As the concentration increases to 1.35 M, the dilute solution turns into a solid gel phase with strong contact ion pairs occurring, suggesting that the strong interactions between hydrated Zn^{2+} cations and −SO$_3^-$ groups of anions contribute to the gel formation. A broad O−H stretching band was observed in the Fourier transform infrared spectra (FTIR) (Figure 2d). This can be attributed to the three

states of water molecules based on their different mean numbers of H-bonds according to earlier studies,[16,17] which respectively are "network water (NW)" (at 3205 cm^{-1}) for which water molecules are with an H-bond coordination number close to four, "intermediate water (IW)" (at 3433 cm^{-1}) for which water molecules are with distorted H bonds and somewhat connected to other water molecules without establishing a fully connected

**ADVANCED
SCIENCE NEWS**

www.advancedsciencenews.com

**ADVANCED
FUNCTIONAL
MATERIALS**

www.afm-journal.de

network, and "multimer water (MW)" (at 3560 cm^{-1}) for which water molecules stand as free monomers/dimers/trimers and are poorly connected to their environment. Compared to the pure water as well as the electrolyte solution <1 M, the signal corresponding to NW at >1 M decrease and signals corresponding to MW and IW increase. Especially after the gel formation, the signal corresponding to NW decreases significantly, suggesting that salts with large anions disrupt the H-bonding network and most water molecules are restrained in the limited framework of the solid gel solution. These account for the high ionic conductivity despite the significantly increased viscosity.

2.2. Zn Plating/Stripping Behaviors in Aqueous Zn(PES)$_2$ Electrolytes

The Zn plating/stripping processes in aqueous Zn(PES)$_2$ electrolytes were evaluated using Zn‖Zn symmetric cells and compared with the conventional aqueous ZnSO$_4$ electrolytes. Figure S3a, Supporting Information compares the voltage profiles of the two different electrolytes at 1 M at different current densities. As can be seen in Figure S3a, Supporting Information, the Zn(PES)$_2$ electrolyte produces smaller polarizations in the Zn‖Zn cell at a wide range of current densities compared to the ZnSO$_4$ electrolyte. This is because the Zn(PES)$_2$ electrolyte offers a higher ionic conductivity as well as a better wettability on Zn metal, which is evidenced by the lower contact angle of the Zn(PES)$_2$ electrolyte on Zn surface shown in Figure S3b, Supporting Information in the Supporting Information. The better wettability of the Zn(PES)$_2$ electrolyte on Zn surface can be attributed to the hydrophobic effect derived from its large hydrophobic anions, driving PES$^-$ anions to self-assemble with the tails toward the Zn anode surface and the polar headgroup exposed to water.[24] As the current density increased to 2 mA cm^{-2}, the cell with the ZnSO$_4$ electrolyte suffered from an open-circuit failure due to severe H$_2$O reduction and limited Zn^{2+} diffusion (Figure S3a, Supporting Information). By contrast, with the Zn(PES)$_2$ electrolyte, good performance was maintained at current densities > 2 mA cm^{-2} (Figure S3a, Supporting Information). The Zn plating/stripping behavior in the Zn(PES)$_2$ electrolyte was then tested at a fixed areal capacity of 0.5 mAh cm^{-2} (Figure S3c, Supporting Information), which further confirmed the good rate performance with the new electrolyte by showing current densities up to 4 mA cm^{-2}. It is noted that Figure S3a,c, Supporting Information show different polarization voltages even at the same current density. This can be attributed to the different activation conditions used in the two measurements. In Figure S3a, Supporting Information, a discharge/charge time of 0.5 h was used, and the areal capacity thus Zn utilization varied with varying current density. In Figure S3c, Supporting Information, the measurement was done under a fixed areal capacity/Zn utilization of 0.5 mAh cm^{-2}. Since the areal capacity in Figure S3a, Supporting Information varied with the highest value double the condition in Figure S3c, Supporting Information; Figure S3, Supporting Information a had a higher Zn utilization, which would create more porous reactive area on the Zn surface. When tested at the same current density, a larger zinc area led to a lower polarization.

The cycling performance of Zn plating/stripping in Zn(PES)$_2$ electrolytes at different concentrations is shown in **Figure 3**. At a high areal capacity of 2 mAh cm^{-2}, the Zn(PES)$_2$ electrolyte at 1 M showed dendrite-free Zn plating/stripping for more than 2500 h at 0.5 mA cm^{-2} and more than 1600 h at 1 mA cm^{-2} (Figure 3a,b). Under an even harsher condition of 2.5 mA cm^{-2} and 5 mAh cm^{-2}, the electrolyte suppresses dendrite growth for over 380 h (Figure 3c). These are the highest values in the electrolyte studies reported to date with such high areal capacities and high current densities. It is noted that the polarization of the symmetric cell grows bigger as the cycling proceeds especially at higher current densities, which can be ascribed to the slow formation of by-products on the Zn anode surface. The X-ray diffraction (XRD) patterns (Figure S4, Supporting Information) show the appearance of a weak peak around 8.4° after 200 h of cycling, indicating the formation of by-products. As the Zn(PES)$_2$ concentration increased to 1.2 M, the cycling performance at 2 mAh cm^{-2} decreased to ≈2000 h at 0.5 mA cm^{-2} and ≈1300 h at 1 mA cm^{-2}, but these values are still beyond most of the published data (Table S1, Supporting Information).[25–29] Figure S5, Supporting Information shows the cycling performance in 1 M Zn(PES)$_2$ electrolyte under most published test conditions (0.5 mAh cm^{-2}, 0.25 mA cm^{-2}), in which more than 7000 h was achieved. A sudden voltage increase is observed at ≈820 h in the long cycling experiment. This is contrary to the voltage drop associated with the "soft circuit" effect,[30] hence, it may be caused by some accidental temporary disconnection in the circuit during the measurement. Figure 3d summarizes the state-of-the-art of aqueous Zn‖Zn cell cycling life as a function of current density and areal capacity per cycle. It can be seen that the present work exceeds all the previous efforts,[15–17,25–29] though most of them were conducted under mild conditions (< 1 mAh cm^{-2}).

2.3. Zn Plating/Stripping Morphology

Scanning electron microscopy (SEM) was used to study the Zn surface after 50 cycles at 0.5 mA cm^{-2} at 0.5 mAh cm^{-2} in a Zn‖Zn cell with 1 M Zn(PES)$_2$. For comparison, the SEM images of the Zn surface cycled in 1 M ZnSO$_4$ under the same conditions are shown in Figure S6, Supporting Information. With the conventional ZnSO$_4$ electrolyte, not surprisingly, uncontrolled dendritic Zn growth was observed, which was responsible for the fast failure of the cell with ZnSO$_4$ electrolytes.[31] By contrast, Zn plating from the Zn(PES)$_2$ electrolyte was compact and smooth as shown in **Figure 4**a,b. The linear indentations on the deposited Zn surface were caused by the fibers of the separator (Figure 4b). The Zn metal surface morphology after longer-term cycles (for 3000 h at 0.25 mA cm^{-2} at 0.5 mAh cm^{-2}) in the Zn(PES)$_2$ electrolyte is shown in Figure S7, Supporting Information, where a dendrite-free and uniform Zn surface is also observed, indicating that dendrite growth is remarkably suppressed in the new electrolyte. A protecting layer can be observed on the unwashed Zn samples after cycling in the Zn(PES)$_2$ electrolyte (Figure 4a,c), which is believed to contribute to the improved Zn reversibility. From the energy dispersive X-ray spectroscopy (EDX) results for the unwashed Zn surfaces (Figure S8, Supporting Information),
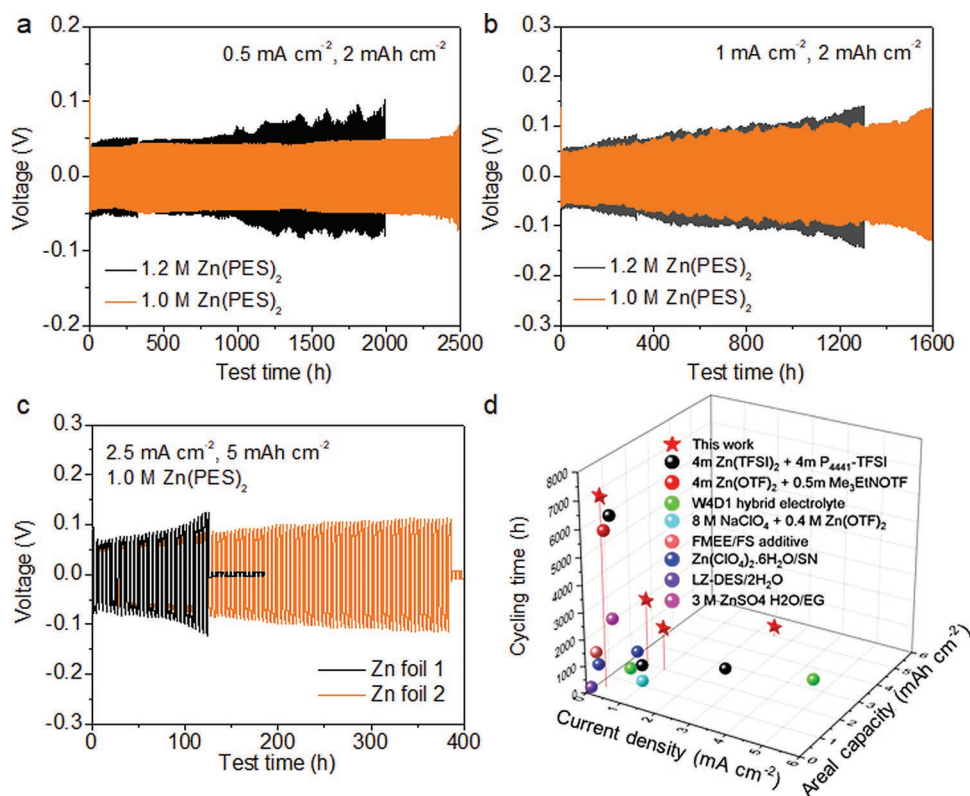
**ADVANCED
SCIENCE NEWS**

www.advancedsciencenews.com

**ADVANCED
FUNCTIONAL
MATERIALS**

www.afm-journal.de

Figure 3. The cycling performance of Zn plating/stripping in $Zn(PES)_2$ electrolytes. a,b) Galvanostatic Zn plating/stripping in different electrolyte concentrations at a) 0.5 mA cm^{-2} at 2 mAh cm^{-2} and b) 1 mA cm^{-2} at 2 mAh cm^{-2}. c) Galvanostatic Zn plating/stripping with different Zn foils (Zn foil 1: 80 μm thick; Zn foil 2: 50 μm thick) in 1 M $Zn(PES)_2$ at 2.5 mA cm^{-2} at 5 mAh cm^{-2}. d) Comparison of cycling times in this work with other studies on aqueous Zn electrolytes at different current densities and areal capacities.[15–17,25–29] The details are as follows. W4D1: 2 M $Zn(OTf)_2$ in H$_2$O/DMC 1/8 (mole ratio);[17] FMEE/FS: 1 M $ZnSO_4$ + 0.005 wt% fatty methyl ester ethoxylate (FMEE) + 4 wt% fumed silica (FS);[29] $Zn(ClO_4)_2·6H_2O$/SN 1/8: $Zn(ClO_4)_2·6H_2O$/succinonitrile 1/8 (mole ratio);[25] LZ-DES/2H$_2$O: LiTFSI/Zn(TFSI)$_2$/urea/H$_2$O (1/0.05/3.8/2 by mole);[27] 3 M $ZnSO_4$ H$_2$O/EG: 3 M $ZnSO_4$/H$_2$O/68 vol% EG.[28]

it was found that the protecting layer was mainly composed of F, S, O, and C elements and the atomic ratio of F:C (9.32:1) was quite close to that of PES$^-$ anions (9:1), indicating that the layer was solidified from the bulk $Zn(PES)_2$ solution due to water reduction at the anode surface during the initial cycles. This is further confirmed through the Raman analysis of a Zn metal surface cycled for 100 h in 1 M $Zn(PES)_2$ at 0.5 mA cm^{-2} at 0.5 mAh cm^{-2}. As shown in Figure 4d, the Raman peak corresponding to the $Zn(PES)_2$ gel phase occurs, and the signal of the 1 M $Zn(PES)_2$ electrolyte almost disappears.

2.4. Electrochemical Properties of the Biomimetic Lipid-Bilayer Gel Layer

The electrochemical stability window of the gel layer was evaluated with Zn‖Ti cells with a $Zn(PES)_2$ gel as an electrolyte. The electrochemical stability window of the dilute $ZnSO_4$ electrolyte was also measured for benchmarking. It can be seen from **Figure 5** that the gel electrolyte not only negatively shifts the Zn^{2+} reduction potential but also decreases the reduction current density from 0.285 to 0.072 mA cm^{-2} at −0.11 V (vs Zn/Zn^{2+}), suggesting better suppression of hydrogen evolution compared to the dilute $ZnSO_4$ electrolyte. In addition, the

gel electrolyte extends the onset potential of oxygen evolution to ≈2.03 V compared to ≈1.97 V for 1 M $ZnSO_4$ when 0.02 mA cm^{-2} is set as the threshold for oxygen evolution. As a result, an electrochemical window of ≈2.16 V with both cathodic (−0.132 V vs Zn/Zn^{2+}) and anodic (2.03 V vs Zn/Zn^{2+}) can be achieved with the gel electrolyte, which can satisfy the voltage requirements of most cathode materials for Zn storage.[32–37] The plating/stripping reversibility of Zn‖Zn symmetric coin cells in the $Zn(PES)_2$ gel electrode was also evaluated. As shown in Figure 5b, the gel electrolyte rendered excellent Zn^{2+} reversibility in Zn‖Zn symmetric cells for over 3000 h at 0.5 mAh cm^{-2} at 0.5 mA cm^{-2}. Even under more aggressive conditions (1 mA cm^{-2}, 1 mAh cm^{-2}), the coin cell still exhibits dendrite-free cycling over 1150 h as shown in Figure S9, Supporting Information. The Zn plating/stripping Coulombic efficiency (CE) with $Zn(PES)_2$ gel was further tested using an asymmetric Zn/Cu coin cell and compared with the CEs with dilute $Zn(PES)_2$ electrolytes (Figure S10, Supporting Information). The CE in $Zn(PES)_2$ gel electrolyte exhibited a sharp increase with the number of cycles and reached >99% within the first five cycles before reaching a plateau. In comparison, the CE values in dilute $Zn(PES)_2$ electrolytes (1, and 1.2 M) experienced a gradual increase and did not reach >99% and the plateau till ≈150 cycles due to the growth of biomimetic gel layers in the
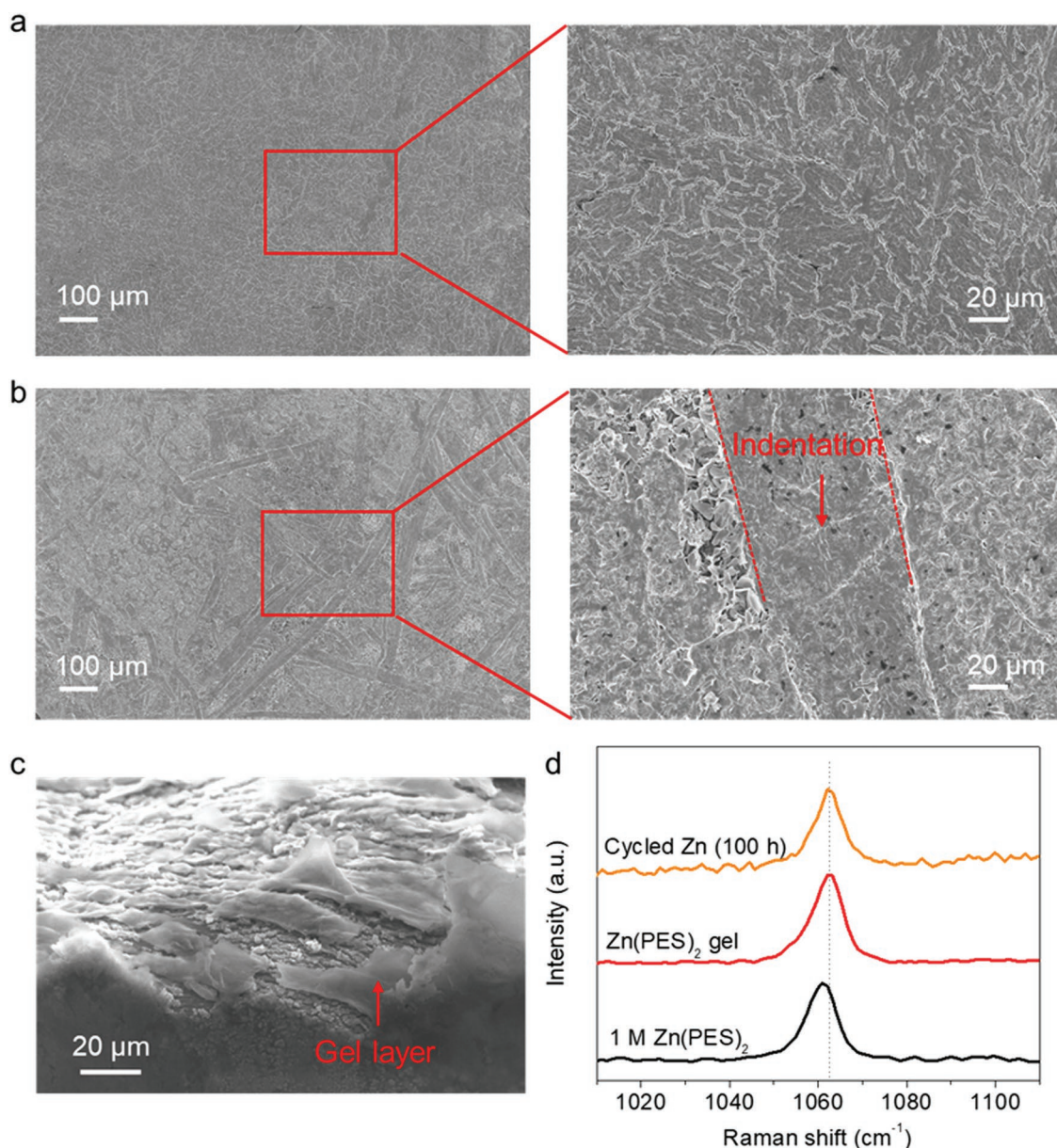
**ADVANCED
SCIENCE NEWS**

www.advancedsciencenews.com

**ADVANCED
FUNCTIONAL
MATERIALS**

www.afm-journal.de

Figure 4. SEM images of Zn metal after 50 plating/stripping cycles in 1 M Zn(PES)$_2$ electrolyte at 0.5 mA cm^{-2} at 0.5 mAh cm^{-2} a) before washing and b) after washing by deionized water. c) Oblique cross-section SEM image. d) Raman spectra of Zn metal surface after 50 plating/stripping cycles at 0.5 mA cm^{-2} at 0.5 mAh cm^{-2} compared with that of 1 M Zn(PES)$_2$ aqueous solution and Zn(PES)$_2$ gel.

dilute electrolytes, suggesting a crucial role of the gel layer in improving Zn reversibility. An average Coulombic efficiency of 99.47% was achieved with Zn(PES)$_2$ gel electrolyte.

2.5. SEI Chemistry

To probe the SEI chemistry, X-ray photoelectron spectroscopy (XPS) was conducted. In the F 1s spectra from XPS (**Figure 6**a–c), signals of inorganic ZnF$_2$ around 684.7 eV and C–F component around 688.6 eV were detected on the cycled Zn. The increasing ZnF$_2$ fraction with increasing Ar$^+$ etching time suggests a higher fluoride content in the inner layer of

the interphase, which agrees with previous studies.[15,16] In the S2p spectrum (Figure 6d), a new peak associated with sulfide appears at 162.4 eV, indicating the decomposition of PES$^-$. This may be caused by the tendency of the hydrophobic parts of PES- anions to replace water near the Zn surface before the interphase formation, which facilitates the interphase formation from PES$^-$ anion reduction and in the mean time suppresses hydrogen evolution. Moreover, as the etching depth increases, the ratio of inorganic fluorine to organic fluorine increases with etching time, while the signal of sulfides decreases, indicating that ZnF$_2$ dominate the inner part of the SEI layer whereas S-rich organic compounds mainly exist in the outer part of the SEI layer. This observation is consistent with
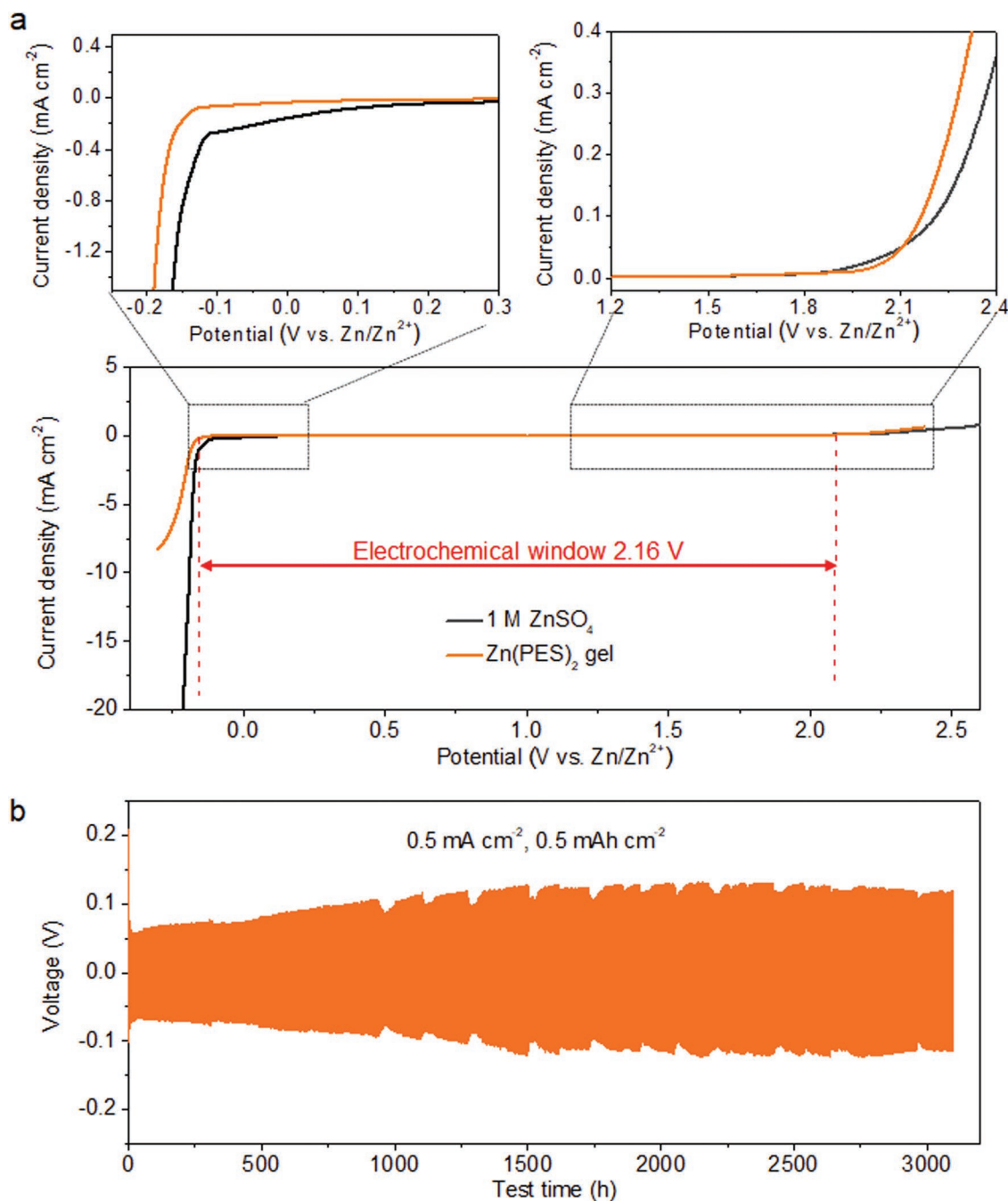
**ADVANCED
SCIENCE NEWS**

www.advancedsciencenews.com

**ADVANCED
FUNCTIONAL
MATERIALS**

www.afm-journal.de

Figure 5. Electrochemical properties of the Zn(PES)$_2$ gel electrolyte. a) The electrochemical stability window in the Zn(PES)$_2$ gel electrolyte compared to that in 1 M ZnSO$_4$. b) Cycling performance in a Zn‖Zn cell with Zn(PES)$_2$ gel electrolyte at 0.5 mA cm^{-2} at 0.5 mAh cm^{-2}.

previous studies.[15,16] Figure 6e shows the transmission electron microscopy (TEM) image of the SEI layer on a Zn surface cycled in a 1 M Zn(PES)$_2$ electrolyte. The SEI-coated Zn anode obtained by cycling in a 1 M Zn(PES)$_2$ electrolyte was then reassembled in a Zn‖Zn cell with 1 M ZnSO$_4$ electrolyte. As shown in Figure 6f, the cycling life with the SEI-coated Zn anode in 1 M ZnSO$_4$ is significantly extended to > 100 h at 0.5 mA cm^{-2} at 0.5 mAh cm^{-2}, suggesting that the SEI formation with the Zn(PES)$_2$ electrolyte also contributes to the resultant long cycling stability.

2.6. Electrochemical Performance of Zn-Metal Full Cells

The new electrolyte was finally tested in a full Zn-ion battery cell consisting of a Zn anode and vanadium sulfide (VS$_2$) deposited on stainless steel (SS) mesh as a cathode (**Figure 7**a). The free-standing VS$_2$@SS cathode was prepared following the procedures in the literature[38] with its XRD and SEM results shown in Figures S11 and S12, Supporting Information. The Zn storage behavior of the prepared VS$_2$@SS cathode was verified through cyclic voltammetry (CV) measurements in 1 M
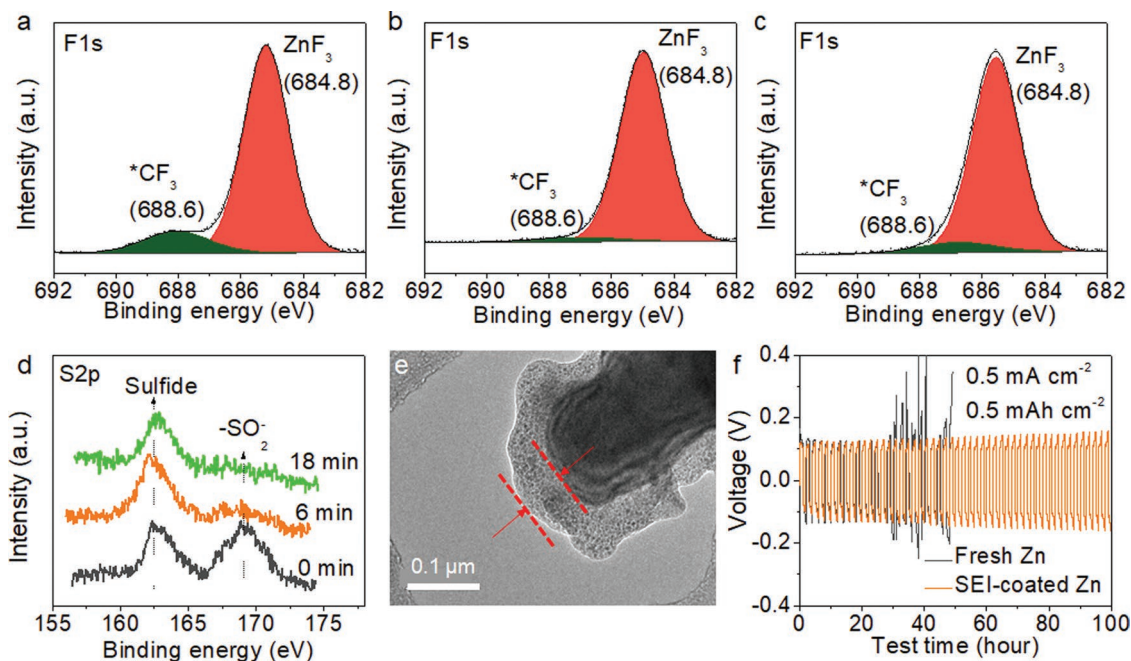
Figure 6. a–d) XPS spectra of C 1s a) 0 min, b) 6 min, c) 18 min, and d) S 2p at various argon (Ar^+) sputtering times on the SEI formed on the Zn surface. e) TEM image of the cycled Zn anode surface. f) Cycling performance in 1 M $ZnSO_4$ with a fresh Zn anode and SEI-coated Zn anode (obtained by dismantling a cycled Zn‖Zn cell with 1 M $Zn(PES)_2$ electrolyte) at 0.5 mA cm^{-2} at 0.5 mAh cm^{-2}.

$Zn(PES)_2$ solution (Figure 7b). Consistent with the literature,[39] two pairs of reduction/oxidation peaks were found respectively at 0.78/0.69 V (vs Zn/Zn^{2+}) and 0.69/0.58 V (vs Zn/Zn^{2+}). After the initial cycle, the subsequent cycles were almost overlapped, showing an excellent cycling stability of the cathode prepared. The $Zn/VS_2@SS$ full cell with 1 M $Zn(PES)_2$ electrolyte exhibits good rate performance by delivering a reversible capacity of 114.4 mAh g^{-1} at 6.4 mA cm^{-2} (Figure 7c,d). The long-term cycling performance of the full cell was evaluated at different current densities (Figure 7e,f). The cell with 1 M $Zn(PES)_2$ delivered an initial specific capacity of 159.1 mAh g^{-1} at 1.6 mA cm^{-2} after 5 activation cycles and operated for over 2000 cycles with 99.96% Coulombic efficiency and a 45.4% capacity retention. At the current density of 0.64 mA cm^{-2}, a higher initial capacity of 171.5 mAh g^{-1} was achieved with 89.1% capacity retention and a 99.93% Coulombic efficiency after 300 cycles. By contrast, at both current densities, the cell with 1 M $ZnSO_4$ suffered from fast failure (350 cycles for 1.6 mA cm^{-2}, and 174 cycles for 0.64 mA cm^{-2}). We further tested the full cell with a high loading of cathode active materials (7.5 mg cm^{-2}), a good capacity retention of 78% was obtained after 1000 cycles at 1.5 mA cm^{-2}. Full cell tests were also conducted with $Zn_xV_2O_5$ nH_2O (ZnVO) nanorods,[28] a cathode material featuring a relatively large voltage window. As shown in Figure S13, Supporting Information, the Zn/ZnVO cell offers a better performance with $Zn(PES)_2$ electrolyte than with $ZnSO_4$ electrolyte. The cell with $Zn(PES)_2$ electrolyte delivered a reversible specific capacity of 174.8 mAh g^{-1} after 1500 cycles. In comparison, the Zn/ZnVO cell with $ZnSO_4$ electrolyte showed a much faster capacity fade with only 56.1 mAh g^{-1} remaining after 1500 cycles. These full cell tests demonstrated that the $Zn(PES)_2$-based electrolyte can be a promising candidate for high-performance Zn-ion batteries.

3. Conclusion

We present a non-concentrated aqueous electrolyte based on an amphipathic salt, $Zn(PES)_2$, for rechargeable Zn batteries. The new electrolyte remarkably improved the Zn reversibility and rate capability through in situ formation of a biomimetic lipid-bilayer anode protecting layer as well as a composite SEI containing both ZnF_2 and organic species. The protecting layer is composed of hydrophobic regions consisting of perfluorinated tails and the hydrophilic regions consisting of H_2O and Zn^{2+} cations which serves as fast transport pathways of Zn^{2+} in the bulk electrolyte. This electrolyte both expanded the electrochemical stability to improve the cycling performance of Zn‖Zn symmetric cells, while retaining high ionic conductivity to ensure low polarization. The stable, Zn^{2+}-conductive fluorinated solid electrolyte interphase (SEI) further enhanced zinc reversibility. The symmetric cell experiments with the new electrolyte achieved a ultralong cycling life of over 7000 h at 0.25 mA cm^{-2} at 0.5 mAh cm^{-2}, over 1600 h at 1 mA cm^{-2} at 2 mAh cm^{-2}, and over 380 h at 2.5 mA cm^{-2} at 5 mAh cm^{-2}. The electrolyte was then tested in Zn-ion battery cells with a $VS_2@SS$ cathode, demonstrating a good capacity retention of 78% after 1000 cycles at 1.5 mA cm^{-2} with a high-loading cathode. This work brings rechargeable aqueous Zn batteries a significant step closer to practical use by enabling high cycle life at high areal capacities and opens a new route for engineering the electrode–electrolyte interface toward next-generation aqueous Zn batteries.

4. Experimental Section

Preparation of Materials: The salt $Zn(PES)_2$ was prepared by mixing perfluoro(2-ethoxyethane)sulfonic acid (>97% purity, Fluorochem)
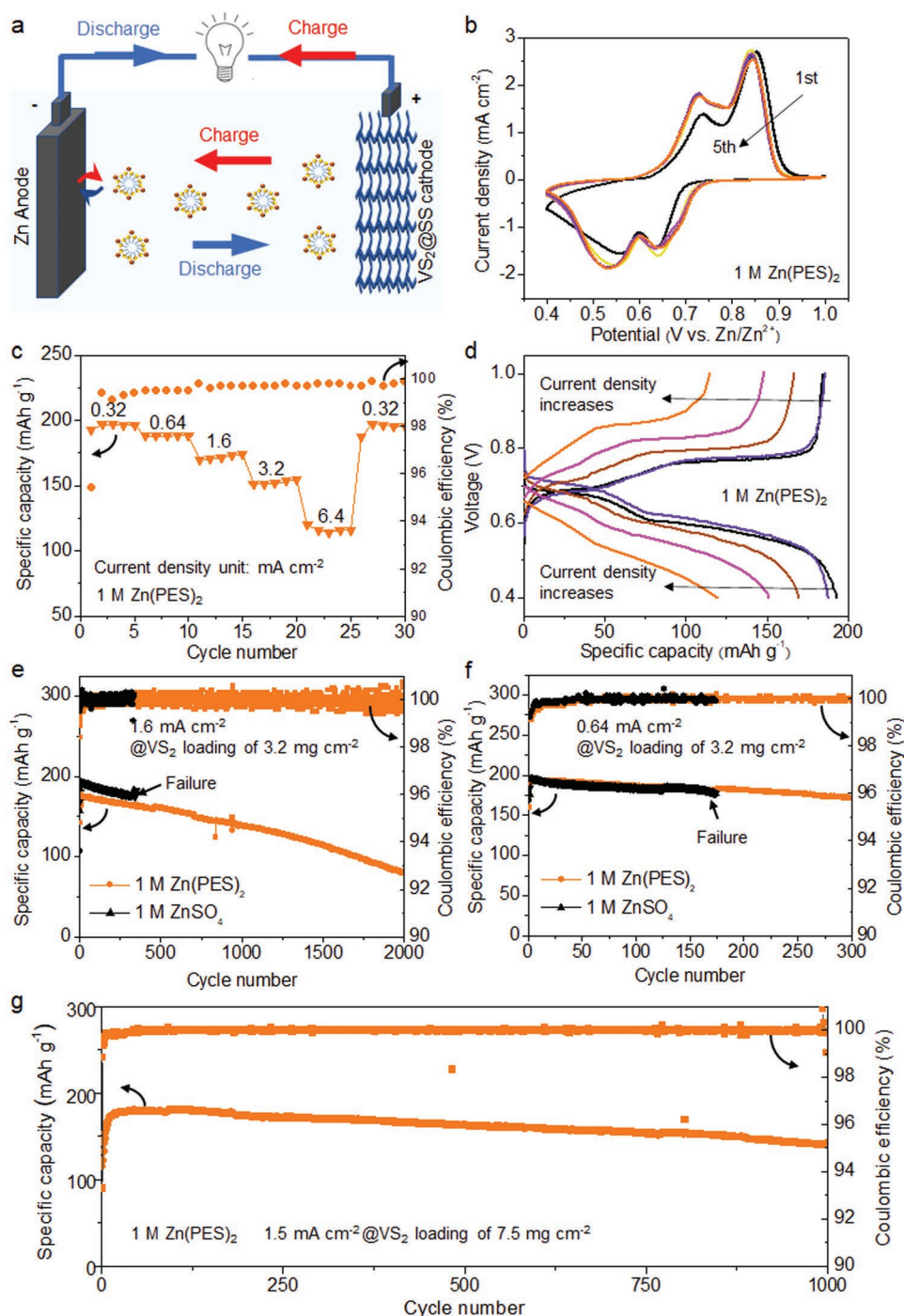
Figure 7. Full cell performance. a) A full Zn-ion battery cell consisting of a Zn anode and a VS$_2$@SS cathode. b) CV curves of a Zn/VS$_2$@SS cell using 1 M Zn(PES)$_2$ at a scan rate of 0.5 mV s^{-1}. c) Rate performance with 1 M Zn(PES)$_2$ and d) its corresponding charge/discharge curves at various current densities (0.32, 0.64, 1.6, 3.2, and 6.4 mA cm^{-2} with a VS$_2$ loading of 3.2 mg cm^{-2}). Cycling performances of full cells with 1 M Zn(PES)$_2$ and 1 M ZnSO$_4$ at e) 1.6 mA cm^{-2} (0.2 A g^{-1} with a VS$_2$ loading of 3.2 mg cm^{-2}) and f) 0.64 mA cm^{-2} (0.5 A g^{-1} with a VS$_2$ loading of 3.2 mg cm^{-2}). g) Cycling performance of a full cell with 1 M Zn(PES)$_2$ electrolyte at a high loading of VS$_2$ at 1.5 mA cm^{-2} (0.2 A g^{-1} with a VS$_2$ loading of 7.5 mg cm^{-2}).

and ZnO (99.9% purity, Sigma–Aldrich) in anhydrous ethanol at room temperature for overnight. The excess ZnO powders were removed by filtration and the remaining solution was dried to obtain white Zn(PES)$_2$ powders. After that, the as-prepared product was redissolved in deionized water to obtain Zn(PES)$_2$ electrolytes, which

were subsequently stored in a dry atmosphere prior to further use. The binder-free cathode VS$_2$@SS was synthesized using a hydrothermal method as detailed in the literature.[38] The Zn||Zn symmetric cells and full cells were assembled in coin cells (CR2032-type) with Zn foils (>99.9 wt% purity, 50 μm thick unless specified, Jianni Lab) as

electrodes and VWR filter paper (≈160 µm) as the separator filled with 100 µL of aqueous electrolytes. Two spacers with thicknesses of 0.5 and 0.8 mm, respectively and a spring with a thickness of 1.1 mm were used to ensure a close contact between different layers of the cell.

Material Characterization and Electrochemical Measurements: Scanning electron microscope (SEM) images were taken using a LEO Gemini 1525 SEM with a high-resolution field emission (FE) gun. The SEI layer was characterized using transmission electron microscopy (TEM) (JEOL-2100 Plus). FTIR measurements were carried out with a Perkin-Elmer spectrometer at an attenuated total reflectance (ATR) mode. The galvanostatic cycling performance was tested using Landt Instruments CT2001A battery cycler systems at different current densities. Cyclic voltammetry (CV) was performed on an electrochemical workstation (Autolab PGSTA302N) to measure the electrochemical stability windows. The powder XRD patterns were obtained by a PANalytical X'Pert X-ray diffractometer with Cu Kα radiation source and a step size of $2\theta = 0.016$ to analyses the crystal structures of the as-received samples. All measurements were conducted at room conditions unless specified.

Supporting Information

Supporting Information is available from the Wiley Online Library or from the author.

Conflict of Interest

The authors declare no conflict of interest.

Data Availability Statement

The data that support the findings of this study are available from the corresponding author upon reasonable request.

[1] IRENA, *Innovation landscape brief: Utility-scale batteries*, International Renewable Energy Agency, Abu Dhabi **2019**, https://www.irena.org/-/media/Files/IRENA/Agency/Publication/2019/Sep/IRENA_Utility-scale-batteries_2019.pdf.

[2] S.-B. Wang, Q. Ran, R.-Q. Yao, H. Shi, Z. Wen, M. Zhao, X.-Y. Lang, Q. Jiang, *Nat. Commun.* **2020**, *11*, 1634.

[3] F. Wang, E. Hu, W. Sun, T. Gao, X. Ji, X. Fan, F. Han, X.-Q. Yang, K. Xu, C. Wang, *Energy Environ. Sci.* **2018**, *11*, 3168.

[4] W. Li, K. Wang, S. Cheng, K. Jiang, *Energy Storage Mater.* **2018**, *15*, 14.

[5] Z. Chen, Q. Yang, F. Mo, N. Li, G. Liang, X. Li, Z. Huang, D. Wang, W. Huang, J. Fan, C. Zhi, *Adv. Mater.* **2020**, *32*, 2001469.

[6] C. Zhang, S. Liu, G. Li, C. Zhang, X. Liu, J. Luo, *Adv. Mater.* **2018**, *30*, 1801328.

[7] B. Tang, L. Shan, S. Liang, J. Zhou, *Energy Environ. Sci.* **2019**, *12*, 3288.

[8] J. Wu, C. Yuan, T. Li, Z. Yuan, H. Zhang, X. Li, *J. Am. Chem. Soc.* **2021**, *143*, 13135.

[9] Y. Cui, Q. Zhao, X. Wu, Z. Wang, R. Qin, Y. Wang, M. Liu, Y. Song, G. Qian, Z. Song, L. Yang, F. Pan, *Energy Storage Mater.* **2020**, *27*, 1.

[10] S. Chen, J. Zheng, L. Yu, X. Ren, M. H. Engelhard, C. Niu, H. Lee, W. Xu, J. Xiao, J. Liu, J.-G. Zhang, *Joule* **2018**, *2*, 1548.

[11] Z. Yu, H. Wang, X. Kong, W. Huang, Y. Tsao, D. G. Mackanic, K. Wang, X. Wang, W. Huang, S. Choudhury, Y. Zheng, C. V. Amanchukwu, S. T. Hung, Y. Ma, E. G. Lomeli, J. Qin, Y. Cui, Z. Bao, *Nat. Energy* **2020**, *5*, 526.

[12] X. Cao, X. Ren, L. Zou, M. H. Engelhard, W. Huang, H. Wang, B. E. Matthews, H. Lee, C. Niu, B. W. Arey, Y. Cui, C. Wang, J. Xiao, J. Liu, W. Xu, J.-G. Zhang, *Nat. Energy* **2019**, *4*, 796.

[13] Z. Zeng, V. Murugesan, K. S. Han, X. Jiang, Y. Cao, L. Xiao, X. Ai, H. Yang, J.-G. Zhang, M. L. Sushko, J. Liu, *Nat. Energy* **2018**, *3*, 674.

[14] H. Qiu, X. Du, J. Zhao, Y. Wang, J. Ju, Z. Chen, Z. Hu, D. Yan, X. Zhou, G. Cui, *Nat. Commun.* **2019**, *10*, 5374.

[15] L. Cao, D. Li, T. Pollard, T. Deng, B. Zhang, C. Yang, L. Chen, J. Vatamanu, E. Hu, M. J. Hourwitz, L. Ma, M. Ding, Q. Li, S. Hou, K. Gaskell, J. T. Fourkas, X.-Q. Yang, K. Xu, O. Borodin, C. Wang, *Nat. Nanotechnol.* **2021**, *16*, 902.

[16] L. Ma, T. P. Pollard, Y. Zhang, M. A. Schroeder, M. S. Ding, A. v Cresce, R. Sun, D. R. Baker, B. A. Helms, E. J. Maginn, C. Wang, O. Borodin, K. Xu, *Angew. Chem., Int. Ed.* **2021**, *60*, 12438.

[17] Y. Dong, L. Miao, G. Ma, S. Di, Y. Wang, L. Wang, J. Xu, N. Zhang, *Chem. Sci.* **2021**, *12*, 5843.

[18] X. Zeng, J. Mao, J. Hao, J. Liu, S. Liu, Z. Wang, Y. Wang, S. Zhang, T. Zheng, J. Liu, P. Rao, Z. Guo, *Adv. Mater.* **2021**, *33*, 2007416.

[19] R. Moshtev, B. Johnson, *J. Power Sources* **2000**, *91*, 86.

[20] S. Xu, G. Szymanski, J. Lipkowski, *J. Am. Chem. Soc.* **2004**, *126*, 12276.

[21] K. Holmberg, *Surfactants*, Wiley-VCH, Weinheim, Germany **2019**, p. 1.

[22] S. Logette, C. Eysseric, P. Huguet, C. Gavach, G. Pourcelly, *J. Appl. Electrochem.* **1999**, *29*, 371.

[23] A. Gruger, A. Régis, T. Schmatko, P. Colomban, *Vib. Spectrosc.* **2001**, *26*, 215.

[24] M. F. Paige, A. F. Eftaiha, *Adv. Colloid Interface Sci.* **2017**, *248*, 129.

[25] W. Yang, X. Du, J. Zhao, Z. Chen, J. Li, J. Xie, Y. Zhang, Z. Cui, Q. Kong, Z. Zhao, C. Wang, Q. Zhang, G. Cui, *Joule* **2020**, *4*, 1557.

[26] F. Wang, O. Borodin, T. Gao, X. Fan, W. Sun, F. Han, A. Faraone, J. A. Dura, K. Xu, C. Wang, *Nat. Mater.* **2018**, *17*, 543.

[27] J. Zhao, J. Zhang, W. Yang, B. Chen, Z. Zhao, H. Qiu, S. Dong, X. Zhou, G. Cui, L. Chen, *Nano Energy* **2019**, *57*, 625.

[28] R. Qin, Y. Wang, M. Zhang, Y. Wang, S. Ding, A. Song, H. Yi, L. Yang, Y. Song, Y. Cui, J. Liu, Z. Wang, S. Li, Q. Zhao, F. Pan, *Nano Energy* **2021**, *80*, 105478.

[29] J. Huang, X. Chi, Q. Han, Y. Liu, Y. Du, J. Yang, Y. Liu, *J. Electrochem. Soc.* **2019**, *166*, A1211.

**ADVANCED
SCIENCE NEWS**

www.advancedsciencenews.com

**ADVANCED
FUNCTIONAL
MATERIALS**

www.afm-journal.de

[30] Q. Li, A. Chen, D. Wang, Z. Pei, C. Zhi, *Joule* **2022**, *6*, 273.

[31] W. Xu, K. Zhao, W. Huo, Y. Wang, G. Yao, X. Gu, H. Cheng, L. Mai, C. Hu, X. Wang, *Nano Energy* **2019**, *62*, 275.

[32] Z. Liu, G. Pulletikurthi, F. Endres, *ACS Appl. Mater. Interfaces* **2016**, *8*, 12158.

[33] P. Hu, M. Yan, T. Zhu, X. Wang, X. Wei, J. Li, L. Zhou, Z. Li, L. Chen, L. Mai, *ACS Appl. Mater. Interfaces* **2017**, *9*, 42717.

[34] W. Sun, F. Wang, S. Hou, C. Yang, X. Fan, Z. Ma, T. Gao, F. Han, R. Hu, M. Zhu, C. Wang, *J. Am. Chem. Soc.* **2017**, *139*, 9775.

[35] F. Wan, L. Zhang, X. Dai, X. Wang, Z. Niu, J. Chen, *Nat. Commun.* **2018**, *9*, 1656.

[36] D. Chao, C. (R.) Zhu, M. Song, P. Liang, X. Zhang, N. H. Tiep, H. Zhao, J. Wang, R. Wang, H. Zhang, H. J. Fan, *Adv. Mater.* **2018**, *30*, 1803181.

[37] V. Soundharrajan, B. Sambandam, S. Kim, V. Mathew, J. Jo, S. Kim, J. Lee, S. Islam, K. Kim, Y.-K. Sun, J. Kim, *ACS Energy Lett.* **2018**, *3*, 1998.

[38] T. Jiao, Q. Yang, S. Wu, Z. Wang, D. Chen, D. Shen, B. Liu, J. Cheng, H. Li, L. Ma, C. Zhi, W. Zhang, *J. Mater. Chem. A* **2019**, *7*, 16330.

[39] J. Liu, J. Long, Z. Shen, X. Jin, T. Han, T. Si, H. Zhang, *Adv. Sci.* **2021**, *8*, 2004689.